Electronic Supplementary information

Combinatorial Alloying Improves Bismuth Vanadate Photoanodes via Reduced Monoclinic Distortion

P. F. Newhouse, D. Guevarra, M. Umehara, S. E. Reyes-Lillo, L. Zhou, D. A. Boyd, S. K. Suram, J. K. Cooper, J. A. Haber, J. B. Neaton, J. M. Gregoire

Comments on Sample Randomization

Duplicate sample sets of the Bi-V-A compositions [which are not shown in Figure 1(a)] and each of the 15 unique Bi-V-A-B sample sets are printed as single or double rows, respectively, whereby the 30 (Bi-V-A) or 60 (Bi-V-A-B) individual compositions are spatially randomized so that any spatial or temporal artifacts with the PEC measurements are not convolved with composition.

Details of Scale-up sample fabrication

To prepare large area films for AM 1.5 measurements a single, 4 cation solution of $Bi_{0.5}V_{0.5}$ with Mo and Gd (1.41% and 3.54%, respectively) was prepared as follows. Dropwise addition of 3.92 mL of 0.268 M $VOSO_4{\cdot}5H_20$ (prepared using a 1:1 mixture of 7.5 vol % HNO_3 with a 15 vol % solution of diethylene glycol in water) to 3.08 mL of 0.341 M $BiNO_3$ (prepared using 7.5 vol % HNO_3) with stirring yielded 7 mL of solution with 0.3 M metal loading. To this solution, 0.25 M $Gd(NO_3)_3$ and 0.25 M $(NH_4)_6Mo_7O_{24}{\cdot}4H_2O$ were added with stirring to produce the desired stoichiometry, followed by filtration using a 0.2 μm filter (Pall Corporation). A 1.5 mL aliquot of this solution was combined with 7.5 uL of Triton (Sigma-Aldrich) surfactant (0.5 vol %) and shaken vigorously before 0.2 mL was pipetted and evenly distributed onto Tec-15 FTO that had been cleaned with soap and water and then dried. After curing in air for 20 min, the sample was spun for 1.2 s at 2000 rpm then placed onto a 40 C hot plate for 5 min before drying for 1 hr in a 60 C oven. Oxide conversion was performed in pure O_2 at 545 C for 30 min.

Details of scaled-up sample under 455 nm illumination

In Figure 2d, the two high performing neighbor samples near the star annotation exhibit an average P_{max} of ~ 1 mW/cm^2. The Bi-V-Mo-Gd scale-up sample from Figs. S1 and S2 was measured in the same experimental measurement configuration but with only 75% of the photon flux used in the combinatorial library measurement. The factor of 1.8 increase of P_{max} in the scaled-up sample compared to the expectation from the high throughput measurements is derived via

$$\frac{[1.35\ \mathrm{mWcm^{-2}}/1\ \mathrm{mW\ cm^{-2}}]}{0.75} = 1.8,$$

Which is similar to the 1.9-fold increase in material loading (average thickness).

Details of determination of maximum photocurrent density via optical absorption of scaled-up samples

Estimates of the idealized maximum photocurrent density based on solar illumination may be determined based on the bandgap of a material but implicitly assume unity absorption, making them pertinent to a given material but not a particular electrode of that material. For $BiVO_4$ where the lowest energy band transition is indirect, ideal absorption necessitates thick samples. However, the low mobility of carriers contradicts ideal absorption constraining samples to be thin where light absorption is not well optimized. We therefore utilize the absorption spectrum of an individual electrode to determine its maximum photocurrent density for a specific illumination condition. Both transmission and reflection spectra were measured using an integrating sphere and a Shimadzu SolidSpec-3700 UV-VIS-NIR spectrophotometer. To account for non-idealities in our lamp spectrum as compared to the standard AM1.5G spectrum, the spectral profile of the Solar Light solar simulator used for the AM1.5G PEC characterizations was recorded using an irradiance calibrated (200-850 nm) Ocean Optics 2000+ fiber coupled spectrometer with a cosine corrector. From this was subtracted the reflection intensity of the quartz window used in the PEC cell as well as absorption of the electrolyte solution at a 1 cm path length. The reflection intensity of the $BiVO_4$ submerged in water was calculated based on the measured reflection intensity in air using the Fresnel equation for the case of normal incidence and the refractive index for water ($\eta_{water} = 1.33$). Shown in Figure S1 is the absorption ($A = 1 - T - R$) of the $BiVO_4$ and $BiVO_4$:(Mo,Gd) samples where R is calculated for the submerged electrode. The maximum photocurrent density was

determined by integrating the product of this fractional absorption and solar simulator spectrum above the bandgap of $BiVO_4$ (E_g = 2.5 eV), which intentionally neglects sub-gap contributions.

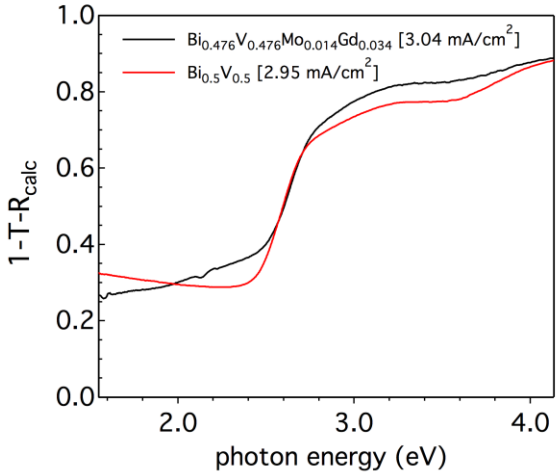

Fig. S1 Absorption spectra for the scaled-up samples derived using measured transmission and reflection spectra collected in air and the reflection intensity was corrected to simulate a submerged electrode by calculation from the Fresnel equation at perpendicular incidence using the index of refraction of water. This absorption spectrum was used to determine the maximum photocurrent density based on the measured Solar Light solar simulator spectrum and accounting for reflection losses at air/quartz window cell and absorption of water in a 1 cm path length. These losses and the band gap value (E_g = 2.5 eV) determine the theoretical maximum photocurrent density for each sample (value in brackets).

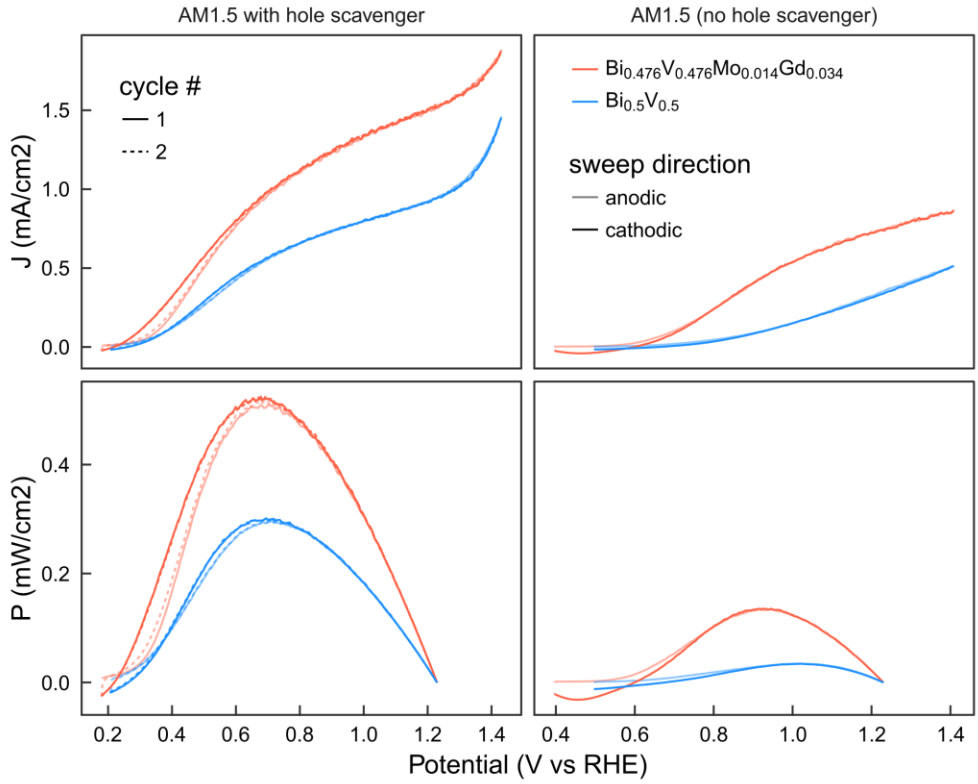

Fig. S2 (upper left) A 2-cycle CV with front-side AM 1.5 illumination (100 mW/cm^2) with sodium sulfite hole scavenger for both

the $Bi_{0.476}V_{0.476}Mo_{0.014}Gd_{0.034}$ sample (area 1.21 cm^2) and a control sample with the same Bi-V ratio but no Mo or Gd (area 1.57 cm^2). (lower left) Photoelectrochemical power density curves calculated as the product of the current density from the CV and the applied potential difference below the OER Nernstian potential. Analogous CV (upper right) and photoelectrochemical power density curves (lower right) without the hole scavenger.

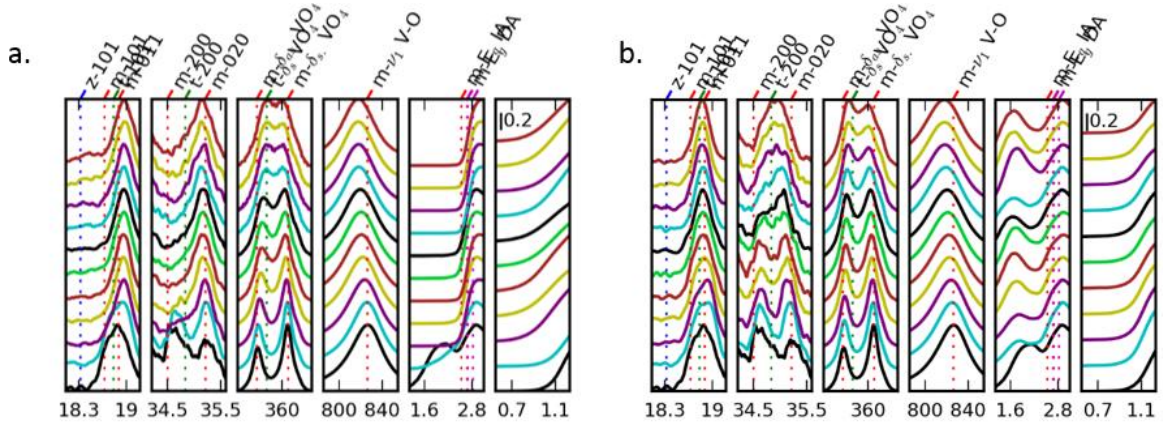

Figure S3. (a) Stack plot representations of the data from Figure 4(c), comprising Bi-V-Gd compositions of $Bi_{0.5}V_{0.5}$:Gd_y, $0 \le y \le 7.8\%$. (b.) Stack plot representations of the data from Figure 4(b), comprising Bi-V-Mo compositions of $Bi_{0.5}V_{0.5}$:Mo_y, $0 \le y \le 7.8\%$. In both figures, the black, lowermost traces correspond to y = 0.

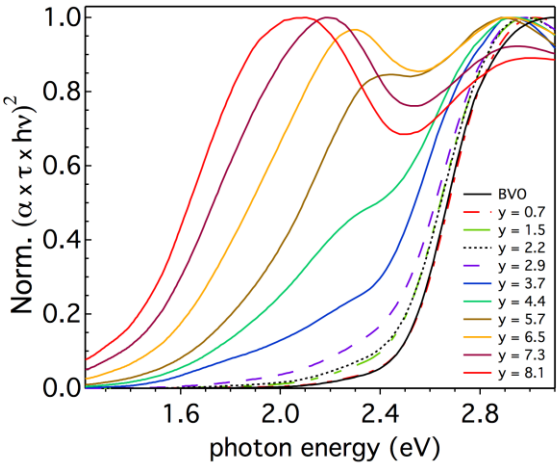

Figure S4. Normalized Direct-Allowed Tauc spectra for a $Bi_{0.52}V_{0.48}$:Mo_y, $0 \le y \le 8.1\%$ sample set.

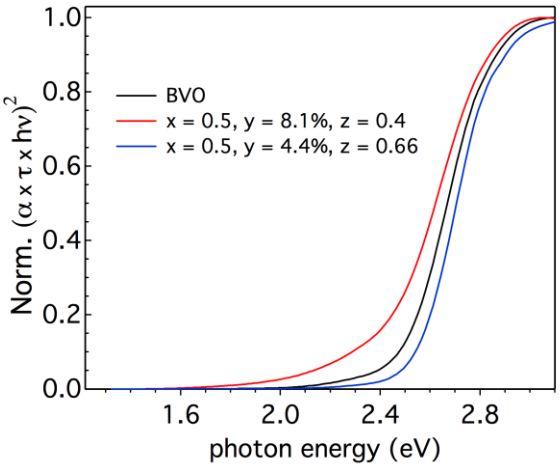

Figure S5. Normalized Direct-Allowed Tauc spectra of the two highest P_{max} compositions in the library together with a non-alloy $Bi_{0.52}V_{0.48}$ control sample. The champion composition (red trace) contains a fractionally large portion of Mo and exhibits sub-gap absorption, consistent with Figure S4. The band gap energy appears consistent within 0.1 eV.

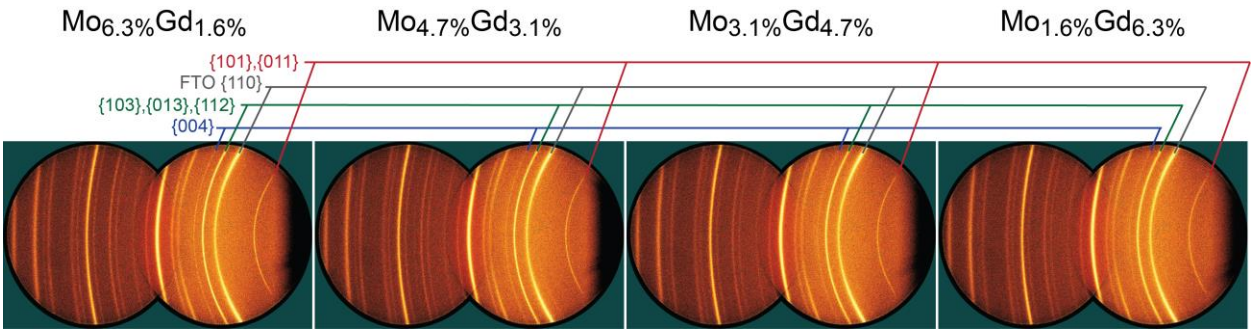

Fig. S6 Two-dimensional diffracted x-ray intensity patterns of four $Bi_{0.5}V_{0.5}$:$(Mo,Gd)_{0.08}$ library samples with noted amounts of Mo/(Bi+V) and Gd/(Bi+V). The colored peak labels correspond to the {*hkl*} for the m-$BiVO_4$ crystal structure, except for the noted FTO {110} peak, and a list of {*hkl*} correspond to multiple overlapped, non-resolved peaks. Respective diffraction rings exhibit uniform intensity along the diffraction ring, indicating no crystallite texturing or preferential growth orientation. The well-separated m-$BiVO_4$ {004} reflection (no overlapped peaks) was used to monitor variation in the grain size for each sample together with the well-separated FTO {110} peak as an internal calibrant.

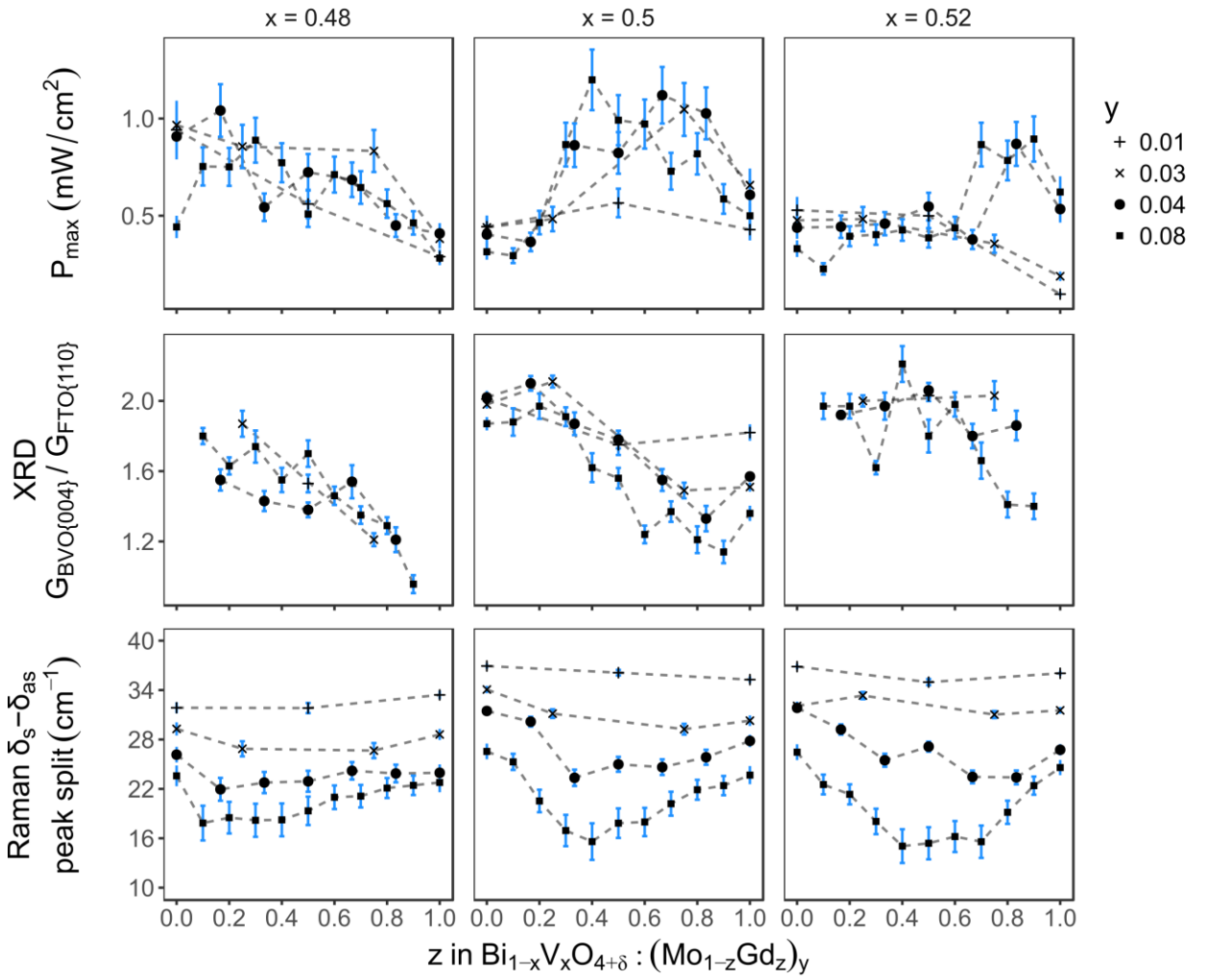

Fig S7. Each row shows the compositional variation of a parameter in the Bi-V-Mo-Gd co-alloying composition space, where each of the 3 horizontal panels have the same layout as Figure 3b. The P_{max} values (top) are the same as Figure 3d with error bars corresponding to the 13% relative error described in the manuscript. The relative peak width (middle) of the m-$BiVO_4$ {004} peak with respect to the FTO {110} peak is inversely related to m-$BiVO_4$ grain size, indicating that the grain size increases slightly with increasing Gd loading. The splitting of the asymmetric (δas) and symmetric (δs) VO_4 bending modes from Raman characterization (bottom) indicates the level of monoclinic distortion. Errors bars for the bottom 2 rows correspond to uncertainty from the fitting procedure, as described in "Details of peak fitting for XRD and Raman data".

Details of peak fitting for XRD and Raman data

We performed pseudo-Voigt function fitting ($f(x)$) on XRD patterns to obtain the peak width for FTO (110) reflection near 26.5° 2θ (W_{FTO}) and the BVO (004) reflection near 30.5° 2θ (W_{BVO}).

$$f(x) = p_1\left(\eta\left(\frac{2}{\pi}\frac{\mathrm{p}_3}{4(x-p_2)^2 + \mathrm{P}_3^2}\right) + (1-\eta)\left(\frac{\sqrt{4\log(2)}}{\sqrt{\pi}\,p_3}\right)\exp\left(-\left(\frac{4\log(2)}{p_3^2}\right)(x-p_2)^2\right)\right).$$

We also obtained standard deviation of the peak width of FTO (110) (E_{FTO}) and BVO (004) (E_{BVO}) from the covariance matrix of peak fitting.

Next, we determined the ratio between the peak width of BVO (004) and averaged peak width of FTO (110), e.g. $\left(W_{\frac{\mathrm{BVO}}{\mathrm{FTO}}}\right)$, and errors $\left(E_{\frac{\mathrm{BVO}}{\mathrm{FTO}}}\right)$ as follows:

$$W_{\frac{\mathrm{BVO}}{\mathrm{FTO}}} = \frac{W_{\mathrm{BVO}}}{W_{\mathrm{FTO,\ ave}}},$$

$$E_{\frac{\mathrm{BVO}}{\mathrm{FTO}}} = \pm W_{\frac{\mathrm{BVO}}{\mathrm{FTO}}} \sqrt{\left(\frac{E_{\mathrm{BVO}}}{W_{\mathrm{BVO}}}\right)^2 + \left(\frac{E_{\mathrm{FTO,\ ave}}}{W_{\mathrm{FTO,\ ave}}}\right)^2},$$

$$W_{\mathrm{FTO,\ ave}} = \frac{1}{n} \Sigma\, W_{\mathrm{FTO}},$$

$$E_{\mathrm{FTO,\ ave}} = \frac{1}{n} \sqrt{\Sigma E_{\mathrm{FTO}}^2}$$

, where n denotes the number of samples.

The data processing of Raman spectra focused on the VO_4 bending mode portion of the spectra and commenced with subtraction of a linear background signal over the wavenumber range of 300 - 400 cm^{-1} as shown in Figure 4. The resulting signal was fit using two independent Lorentz function by least square method;

$$f(x) = p_1 \frac{1}{(x - p_2)^2 + {p_3}^2} + p_4 \frac{1}{(x - p_5)^2 + {p_6}^2}$$

where x is wavenumber and p_i $(i = 1,2,3,4,5,6)$ are fitting coefficients. The peak position of the double-peak is represented by p_2 and p_5. A typical fitted plot is shown below, where the Lorentzian line shape does not completely model the peak tails but provides an excellent fit for determining the peak splitting. The error in fitting parameters is analogous to that described for XRD fitting above.

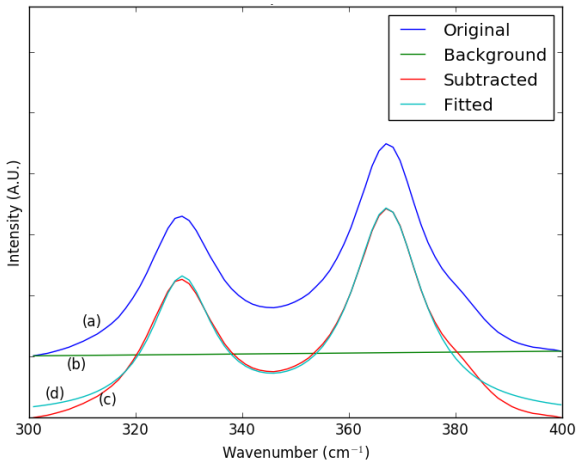

Fig. S8 Lorentz function fitting of a typical library sample. (a) original spectrum, (b) background signal, (c) background-subtracted spectrum, and (d) fitted spectrum with two Lorentz functions. While the tails of the Raman signal are not perfectly modelled by the Lorentzian line shape, this simple fitting model nicely captures the peak splitting and its compositional trend.

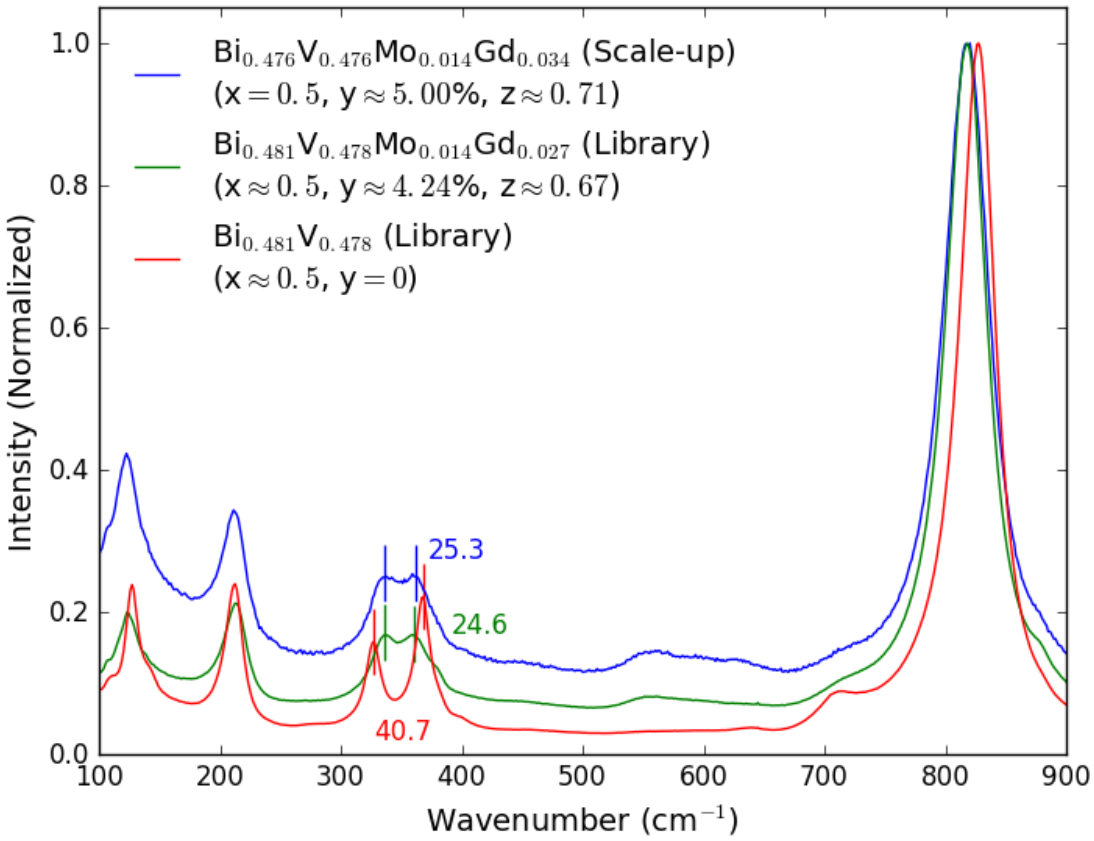

Fig S9 Normalized Raman patterns for a Bi-V library sample (red), a high-performing library sample with composition similar to the scale-up composition (green), and the scale-up sample from Figs S1 and S2. The Raman pattern of the scaled-up sample matches that of the Bi-V-Mo-Gd library sample, demonstrating the reduced monoclinic distortion in the scaled-up sample. The splitting of the asymmetric (δas) and symmetric (δs) VO_4 bending modes in cm^{-1} is labeled for each Raman pattern, and using Eq. 2 the corresponding monoclinic aspect ratios are 1.020 for the Bi-V sample and 1.012 for the Bi-V-Mo-Gd samples.

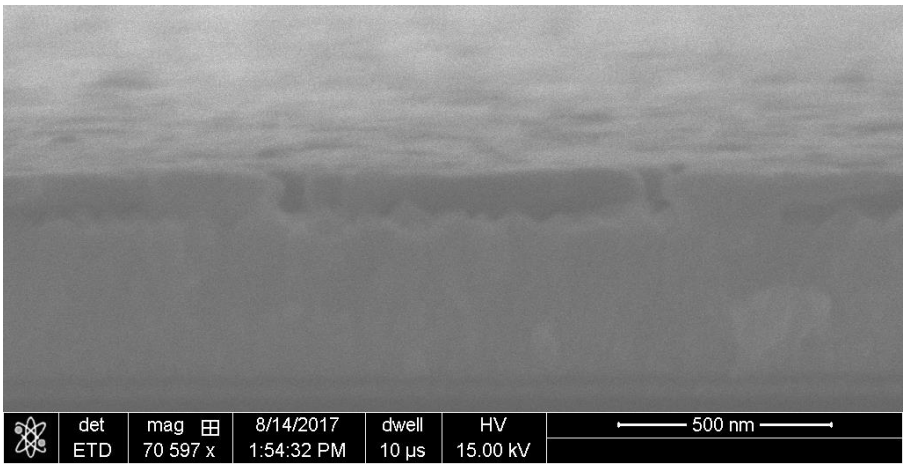

Figure S10. Cross sectional SEM image of an ink jet sample where the top layer is the Bi-V oxide and the underlying layer is the FTO conduction layer.

DFT Calculation of Structures with Degrees of Monoclinic Distortion

We start by performing full structural relaxation with DFT-HSE (with a large α, see below) of the t-$BiVO_4$ and m-$BiVO_4$ phases. Table S1 shows that computed lattice parameters are in good agreement with experimental values.

Table S1. Computed energy difference and lattice parameters for tetragonal and monoclinic $BiVO_4$ using the HSE functional and α = 50%.

HSE-relaxed structure	Energy wrt hull (meV/f.u.)	Lattice param.	This work	Prev work[1]	Experiment (295K) [2]
Tetragonal	4	a (Å)	5.064	5.076	5.147
		b (Å)	11.474	11.521	11.722
Monoclinic	0	a (Å)	5.113	5.197	5.194
		b (Å)	5.025	5.006	5.090
		c (Å)	11.518	11.722	11.697
		γ (°)	90.30	90.81	90.39

We compute the m-$BiVO_4$ phase to have the lowest energy, in agreement with experiments.[2] In our calculations, the t-$BiVO_4$ phase is 4 meV per formula unit above m-$BiVO_4$. As has been pointed out previously, a large value of α is required to properly describe the energetic ordering of the structures and the monoclinic lattice of m-$BiVO_4$.[1]

The higher symmetry t-$BiVO_4$ structure can be seen to be related to the lower symmetry m-$BiVO_4$ structure through the combined effect of two zone-center (q = 0) optical modes with Γ^+_1 and Γ^+_2 symmetry. Γ^+_2 corresponds to the primary order parameter of the ferroelastic transition and originates the monoclinic lattice distortion. Γ^+_1 corresponds to a small uniform expansion of the unit cell, and is not discussed further. As shown in Fig. 1, the Γ^+_2 mode can be further decomposed into two optical modes with Γ^+_2 symmetry,[3] here denoted as $\Gamma^+_{2,xy}$ and $\Gamma^+_{2,z}$. $\Gamma^+_{2,xy}$ denotes the stretching and contraction of the VO_4 tetrahedron edges within the (001) planes, and $\Gamma^+_{2,z}$ denotes the anti-polar displacements of the (001) layers along the [001] direction.

Table S2 shows the real space pattern displacement and mode amplitudes for $\Gamma^+_{2,xy,z}$. Mode amplitudes are computed with respect to eigenvectors normalized to 1Å. Our DFT-HSE calculations underestimate experimental mode amplitudes due to limitations of the approximate exchange-correlation functional.[1] In what follows, we interpolate between the t-$BiVO_4$ and m-$BiVO_4$ structures by linearly varying the amplitude of the Γ^+_2 mode from 0 (t-$BiVO_4$) to its value in the relaxed m-$BiVO_4$ structures (denoted as "1 (m)" in Fig. 6). In addition, we extrapolate the monoclinic distortion beyond the m-$BiVO_4$ structure by considering larger mode amplitudes. Table S3 reports the space group, Wyckoff atomic coordinates, lattice parameters and volume of the interpolated structures.

Table S2**:** Atom displacements for the eigenvectors that describe the monoclinic distortion with respect to the higher-symmetry tetragonal scheelite structure in $BiVO_4$. Q is the eigenvector amplitude (or norm of the mode), which is computed directly from atomic positions

Atom	$\Gamma^+_{2,xy}$		$\Gamma^+_{2,z}$
	x	y	z
Bi	0	0	$u_{Bi,x}$
V	0	0	$u_{V,x}$
O_1	$u_{O,x}$	$-u_{O,y}$	$u_{O,z}$
O_2	$u_{O,x}$	$u_{O,y}$	$u_{O,z}$
Q_{exp}	0.21		0.20
Q_{theo}	0.10		0.12

Table S3: For each interpolated structure we report the space group, Wyckoff positions, lattice parameters and volume.

Structure	Space group	Wyckoff positions	Lattice parameters (Å) and angles(°)	Volume Å^3
0	I41/b	Bi(4a) V(4b) O(16f) x = 0.2491, y = 0.1116, z = 0.0464	a=5.0640 b=5.0640 c=11.4743	294.22
1	C2/c	Bi(4e) y = 0.3778 V(4e) y = -0.1232 O_1(8f) x = -0.2531, y = 0.0448, z = -0.3625 O_2(8f) x = 0.3636, y = 0.2984, z = -0.1321	a=7.1586 b=11.4849 c=5.0761 γ=135.0879	294.65
2	C2/c	Bi(4e) y = 0.3806 V(4e) y = -0.1214 O_1(8f) x = -0.2552, y = 0.0432, z = -0.3625 O_2(8f) x = 0.3658, y = 0.3003, z = -0.1266	a=7.1559 b=11.4958 c=5.0884 γ=135.1757	295.08
3	C2/c	Bi(4e) y = 0.3834 V(4e) y = -0.1196 O_1(8f) x = -0.2573, y = 0.0416, z = -0.3625 O_2(8f) x = 0.3680, y = 0.3023, z = -0.1211	a=7.1531 b=11.5066 c=5.1008 γ=135.2636	295.50
4	C2/c	Bi(4e) y = 0.3861 V(4e) y = -0.1178 O_1(8f) x = -0.2594, y = 0.0400, z = -0.3625 O_2(8f) x = 0.3701, y = 0.3043, z = -0.1156	a=7.1505 b=11.5180 c=5.1131 γ=135.3515	295.92
5	C2/c	Bi(4e) y = 0.3889 V(4e) y = -0.1160 O_1(8f) x = -0.2614, y = 0.0383, z = -0.3626 O_2(8f) x = 0.3723, y = 0.3062, z = -0.1101	a=7.1478 b=11.5284 c=5.1254 γ=135.4393	296.34
6	C2/c	Bi(4e) y = 0.3917 V(4e)y = -0.1143 O_1(8f) x = -0.2635, y = 0.0367, z = -0.3626 O_2(8f) x = 0.3745, y = 0.3082, z = -0.1045	a=7.1451 b=11.5393 c=5.1377 γ=135.5272	296.76

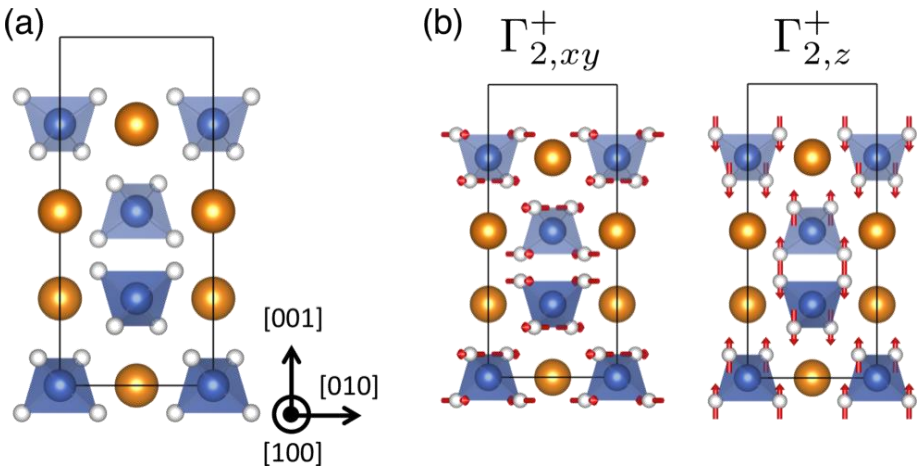

Figure S11. Conventional unit cell for scheelite $BiVO_4$. Bi, V, and O atoms are shown with orange, blue and white spheres (a). Real space pattern displacement for $\Gamma^+_{2,xy}$ and $\Gamma^+_{2,z}$ lattice modes relating t-$BiVO_4$ and m-$BiVO_4$ structures (b). For simplicity, we display the displacement of oxygen atoms only.

Table S4. Electron and hole polaron formation energies for t-$BiVO_4$ and m-$BiVO_4$. Formation energies are computed as the difference between the relaxed polaron and reference states, both calculated using the HSE (α=50%) functional and a 2x2x1 supercell (16 formula unit). While the large value of α may overestimate the absolute formation energies, the accurate description of the ground state properties using this functional indicates that the relative difference between polaron formation energies in t-$BiVO_4$ and m-$BiVO_4$ structures is accurate, in particular that the monoclinic distortion slightly destabilizes electron polarons and slightly stabilizes hole polarons.

Structure	Electron Polaron Formation Energy (eV)	Hole Polaron Formation Energy (eV)
t-$BiVO_4$	-3.07	-1.18
m-$BiVO_4$	-3.05	-1.22
Polaron formation energy of m-$BiVO_4$ compared to t-$BiVO_4$	+1%	-3%

DFT Calculations of Supercells with Site Defects

The effect of Gd, Mo, and W substitutional defects, as well as the co-alloying with composition $Gd_{0.03}Bi_{0.47}Mo_{0.03}V_{0.47}$, are explored by stoichiometric substitution of single atoms in a large supercell with 16 formula units. Our calculations used an energy cut-off of 400 eV, a single Γ point sampling and PAW pseudopotentials with 18, 6, 6 valence electrons for Gd, Mo and W, respectively. Full structural relaxation of atomic positions, volume and lattice parameters are performed until forces are smaller than 0.05 eV/Å with the DFT-HSE exchange-correlation functional. Partial density of states (PDOS) and band structure calculations are computed for the relaxed supercell structure using the Hubbard U corrected GGA functional (DFT+U)[4] with the rotationally invariant method of Dudarev et al. [5]. The Hubbard U values are chosen as U = 4.5 eV for Gd-*f* and U = 3.5 eV for Mo-*d* states, in agreement with standard values in the literature[6]. Since the band gap of the system increases with increasing values of U, we consider rather conservative values of U to underestimate its effect in the position of Gd-*f* electrons in the valence bands. [6]

Table S5 shows the pristine and doped structures considered in this work. For each of the doping and alloying structure we report the supercell structure, composition, DFT-HSE volume change and DFT-HSE relaxed lattice parameters. While the calculations described in the manuscript directly address the primary parameter of interest, the monoclinic distortion, the present calculations for the monoclinic phase provide an independent assessment of the role of the compositional aspect of co-alloying in the structural and electronic properties of monoclinic $BiVO_4$.

Table S5: Pristine and doped structures considered in this work. For each case, we report the supercell structure, composition, DFT-HSE volume change with respect to bulk, and DFT-HSE relaxed lattice parameters and lattice angles.

Structure	Supercell	Composition	ΔV(%)	Lattice parameters (Å)	Lattice Angles (°)
Bulk	$Bi_{16}V_{16}O_{64}$	$Bi_{0.5}V_{0.5}$	0	a = 10.2282 b = 11.5176 c = 10.0502	α = 90.0000 β = 89.6928 γ = 90.0000
1Bi->1Gd	$Gd_1Bi_{15}V_{16}O_{64}$	$Gd_{0.03}Bi_{0.47}V_{0.5}$	-0.8	a = 10.1003 b = 11.3899 c = 10.0116	α = 90.0000 β = 89.8446 γ = 90.0000
1V->1Mo	$Bi_{16}Mo_1V_{15}O_{64}$	$Bi_{0.5}Mo_{0.03}V_{0.47}$	-0.2	a = 10.0987 b = 11.3551 c = 10.0205	α =90.0000 β = 89.8094 γ = 90.0000
1V->1W	$Bi_{16}W_1V_{15}O_{64}$	$Bi_{0.5}W_{0.03}V_{0.47}$	0.1	a = 10.0777 b = 11.3561 c = 10.0395	α = 90.0000 β = 89.9470 γ = 90.0000
1Bi->1Gd, 1V -> 1Mo	$Gd_1Bi_{15}Mo_1V_{15}O_{64}$	$Gd_{0.03}Bi_{0.47}Mo_{0.03}V_{0.47}$	-1.3	a = 10.0736 b = 11.3494 c = 10.0322	α = 89.9915 β = 89.9434 γ = 90.0084

We first consider the effect of Gd, Mo, and W substitutional defects in the structural properties of monoclinic $BiVO_4$ in the dilute limit. We assume a large separation between defects, and therefore we do not treat multiple configurations. Since both Bi and both V atoms have equivalent Wyckoff positions, we consider the following situations: a supercell with a single Gd atom replacing 1 Bi atom; a supercell with a single Mo atom replacing a V atom; a supercell with a single W atom replacing a V atom and a supercell with simultaneous replacing of 1 Gd atom with 1 Bi atom and 1 Mo atom with 1 V atom. Table S6 shows the effect of atomic substitution on the local symmetry (bond lengths) of the monoclinic structure in each case. Our calculations show that independent doping with Gd, Mo, and W all increase the tetragonality of monoclinic BiVO4, in line with our experimental results for simultaneous (Gd,Mo) co-doping of BiVO4. Consequently, we find a larger increase in tetragonality for the combined (Gd,Mo) co-doped structure that for Gd-only and Mo-only doped structures.

Next, we compare the electronic properties of the stoichiometric compositions $Gd_{0.03}Bi_{0.47}V_{0.5}$ and $Gd_{0.03}Bi_{0.47}Mo_{0.03}V_{0.47}$ to explore the effect of Gd and (Gd,Mo) alloying in the electronic properties of monoclinic $BiVO_4$. In our calculations, Gd includes explicitly 18 valence electrons (Gd: $5s^2\ 5p^6\ 4f^7\ 5d^1\ 6s^2$), including *f* electrons. The nominal oxidation states of Gd and Mo are Gd^{+3} and Mo^{+6}, respectively. When substituting Mo for V in our calculations, one electron is removed (and a positive uniform background charge is added) to balance charge and model the anticipated physical scenario for a heterovalent substitution, namely in this case where continues to be Mo^{+6}. Figure S12 shows the PDOS constructed for the supercell substitutional Gd defect ($Gd_1Bi_{15}V_{16}O_{64}$) and the simultaneous substitutional Gd and Mo defects ($Gd_1Bi_{15}Mo_1V_{15}O_{64}$). In both case, we find that in the valence band, Gd *f* electrons lie below 2 eV and mostly near 4 eV below the band edge.

Table S6: Atomic bond lengths for pristine and doped structures. For each case, we report the bond lengths around the defect and the average around the Bi and V atoms. The asymmetry is related to the degree of monoclinic distortion and is computed as the difference between the maximum and minimum bond length. The Bi-O asymmetry values are in bold as these are the primary results discussed in the manuscript

Structure	Bi-O and V-O bond lengths (< > means average)	Asymmetry: max-min
Bulk	<Bi-O>: 2.556(x2) 2.452(x2) 2.364(x2) 2.355(x2)	**0.201**
	<V-O>: 1.728(x2) 1.677(x2)	0.051
1Bi->1Gd	<Bi-O>: 2.467 (x2) 2.406 (x2) 2.379(x2) 2.366 (x2)	**0.101**
	Gd-O: 2.400(x2) 2.391(x2) 2.366(x2) 2.361(x2)	0.039
	<V-O>: 1.708(x2) 1.686(x2)	0.022
1V->1Mo	<Bi-O>: 2.453(x2) 2.413(x2) 2.378(x2) 2.353(x2)	**0.100**
	<V-O>: 1.704(x2) 1.689(x2)	0.015
	Mo-O: 1.764(x2) 1.762(x2)	0.002
1V->1W	<Bi-O>: 2.446(x2) 2.414(x2) 2.382(x2) 2.355(x2)	**0.091**
	<V-O>: 1.702(x2) 1.691(x2)	0.011
	W-O: 1.767(x2) 1.757(x2)	0.010
1Bi->1Gd, 1V -> 1Mo	<Bi-O>: 2.448 (x2) 2.413 (x2) 2.381(x2) 2.353 (x2)	**0.095**
	Gd-O: 2.388(x2) 2.386(x2) 2.363(x2) 2.354(x2)	0.034
	<V-O>: 1.702(x2) 1.691(x2)	0.011
	Mo-O: 1.767(x2) 1.758(x2)	0.009

Figure S12 shows the DFT-GGA band structures for the fully relaxed supercell structures with $Gd_1Bi_{15}V_{16}O_{64}$ and $Gd_1Bi_{15}Mo_1V_{15}O_{64}$ stoichiometries. (Note, as mentioned before, structural optimizations are performed with DFT-HSE; band structures are obtained with DFT-GGA, a lower level of theory that reduces computational expense but, in this case, preserves the trends central to our conclusions.) The valence bands, in particular the regions near the VBM contributing to its effective hole mass, are largely unchanged in the co-alloying composition compared to bulk. The conduction bands are somewhat different and are shifted to lower energy by approximately 0.3 eV, which is primarily due to a volume effect since the Gd and Mo substitution modifies the atomic radii. Since the Gd-*f* electrons are approximately 4 eV below the Fermi level, they do not play a role in the electronic character of the band edges.

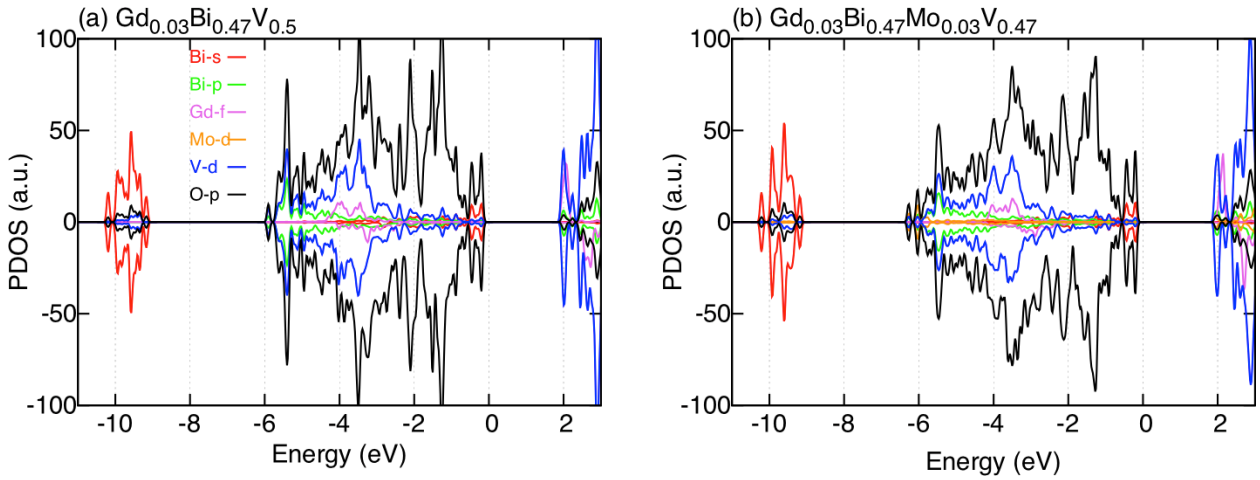

Figure S12: Partial density of states (PDOS) for the supercell structures containing (a) $Gd_{0.03}Bi_{0.47}V_{0.5}$: 1 Gd defect (1 Gd atom replacing 1 Bi atom), and (b) $Gd_{0.03}Bi_{0.47}Mo_{0.03}V_{0.47}$: 1 Gd defect and 1 Mo defect (1 Gd atom replacing 1 Bi atom and 1 Mo atom replacing 1 V atom). PDOS are computed with the DFT-GGA exchange-correlation functional using the relaxed structures obtained with the DFT-HSE exchange-correlation functional. Up and won panels correspond to spin-up and spin-down. The Gd-*f* electrons are included explicitly in the calculation as valence electrons. The zero of energy is set at the highest occupied state.

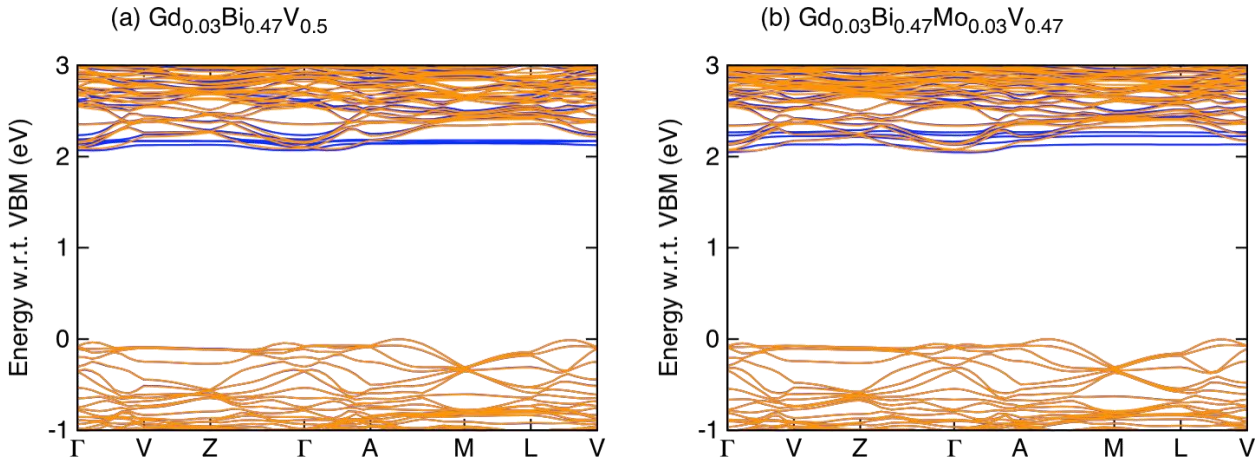

Figure S13: Band structures for the supercell structures (a) $Gd_{0.03}Bi_{0.47}V_{0.5}$: 1 Gd defect (1 Gd atom replacing 1 Bi atom), and (b) $Gd_{0.03}Bi_{0.47}Mo_{0.03}V_{0.47}$: 1 Gd defect and 1 Mo defect (1 Gd atom replacing 1 Bi atom and 1 Mo atom replacing 1 V atom). Band structures are computed with the DFT-GGA exchange-correlation functional using the relaxed structures obtained with hybrid DFT-HSE exchange-correlation functional. Spin-up and spin-down bands are denoted in blue and orange, respectively. The zero of energy is set at the highest occupied state.

References

1. K. E. Kweon and G. S. Hwang, *Physical Review B*, 2012, **86**, 165209.
2. A. W. Sleight, H. Y. Chen, A. Ferretti and D. E. Cox, *Mater. Res. Bull.*, 1979, **14**, 1571-1581.
3. W. I. F. David, A. M. Glazer and A. W. Hewat, *Phase Transitions*, 1979, **1**, 155-169.
4. I. A. Vladimir, F. Aryasetiawan and A. I. Lichtenstein, *Journal of Physics: Condensed Matter*, 1997, **9**, 767.
5. S. L. Dudarev, G. A. Botton, S. Y. Savrasov, C. J. Humphreys and A. P. Sutton, *Physical Review B*, 1998, **57**, 1505-1509.
6. L. Bjaalie, A. Verma, B. Himmetoglu, A. Janotti, S. Raghavan, V. Protasenko, E. H. Steenbergen, D. Jena, S. Stemmer and C. G. Van de Walle, *Physical Review B*, 2015, **92**, 085111.